Circular dichroism in molecular-frame photoelectron angular distributions in the dissociative photoionization of H_2 and D_2 molecules

J. F. Pérez-Torres,[1,*] J. L. Sanz-Vicario,[2,†] K. Veyrinas,[3] P. Billaud,[3,‡] Y. J. Picard,[3] C. Elkharrat,[3] S. Marggi Poullain,[3,§] N. Saquet,[3,‖] M. Lebech,[4] J. C. Houver,[3] F. Martín,[1,5] and D. Dowek[3]

[1]*Departamento de Química, Módulo 13, Universidad Autónoma de Madrid, 28049 Madrid, Spain*

[2]*Grupo de Física Atómica y Molecular, Instituto de Física, Universidad de Antioquia, Medellín, Colombia*

[3]*Institut des Sciences Moléculaires d'Orsay, Université Paris-Sud et CNRS, Batiment 210-350, Université Paris-Sud, F-91405 Orsay Cedex, France*

[4]*Niels Bohr Institute, University of Copenhagen, Copenhagen, Denmark*

[5]*Instituto Madrileño de Estudios Avanzados en Nanociencia (IMDEA-Nanociencia), Cantoblanco, 28049 Madrid, Spain*

(Received 25 July 2014; published 28 October 2014)

The presence of net circular dichroism in the photoionization of nonchiral homonuclear molecules has been put in evidence recently through the measurement of molecular-frame photoelectron angular distributions in dissociative photoionization of H_2 [Dowek *et al.*, Phys. Rev. Lett. **104**, 233003 (2010)]. In this work we present a detailed study of circular dichroism in the photoelectron angular distributions of H_2 and D_2 molecules, oriented perpendicularly to the propagation vector of the circularly polarized light, at different photon energies (20, 27, and 32.5 eV). Circular dichroism in the angular distributions at 20 and to a large extent 27 eV exhibits the usual pattern in which inversion symmetry is preserved. In contrast, at 32.5 eV, the inversion symmetry breaks down, which eventually leads to total circular dichroism after integration over the polar emission angle. Time-dependent *ab initio* calculations support and explain the observed results for H_2 in terms of quantum interferences between direct photoionization and delayed autoionization from the $\mathcal{Q}_1$ and $\mathcal{Q}_2$ doubly excited states into ionic states ($1s\sigma_g$ and $2p\sigma_u$) of different inversion symmetry. Nevertheless, for D_2 at 32.5 eV, there is a particular case where theory and experiment disagree in the magnitude of the symmetry breaking: when D^+ ions are produced with an energy of around 5 eV. This reflects the subleties associated to such simple molecules when exposed to this fine scrutiny.

DOI: 10.1103/PhysRevA.90.043417 PACS number(s): 33.80.Eh, 42.65.Re

I. INTRODUCTION

Photoelectron angular distributions of molecules are useful to obtain information about the electronic dynamics in photoionization, including the interplay between electronic and nuclear motions. Those arising from randomly oriented diatomic molecules in gas phase, depending only on two spherical harmonics, were the subject of early theoretical investigations [1,2]. For molecules with a well-defined orientation, angular distributions are much more complex [2] but provide very detailed information on the dynamics of processes such as dissociative photoionization (DPI). Experiments in the gas phase in which the orientation of the molecule at the time of photoejection is fully determined are feasible in current laboratories, thanks to multicoincidence detection techniques such as reaction microscopes [3] or vector correlation methods [4,5]. When these techniques are applied to DPI of diatomic molecules [$AB + \hbar\omega(\hat{\boldsymbol{\epsilon}}_p) \rightarrow A^+ + B + e^-$], the triplet of vectors ($\mathbf{V}_{A^+}, \mathbf{V}_e, \hat{\boldsymbol{\epsilon}}_p$) corresponding to the velocity of the ionic fragment, the velocity of the ejected electron, and the field polarization axis, respectively, can be measured in coincidence for each DPI event. Therefore, they allow one to obtain a complete kinematical description of the ionization dynamics for oriented or fixed-in-space molecules in the gas phase.

Circular dichroism (CD) represents the different response of a system when exposed to left and right circularly polarized light. CD in photoabsorption of chiral molecules, i.e., without a plane or center of symmetry, is an effect of optical activity already known since its discovery by Pasteur [6]. For such species, the study of photoelectron circular dichroism (PECD) has encountered numerous developments in recent years and has been demonstrated to be a direct and orbital-sensitive chiroptical probe of static and dynamical molecular structures (see [7] and references therein). Recent applications address the determination of absolute molecular stereochemistry in the gas phase [8]. Nonchiral molecules, like diatomic molecules, may also show particular asymmetries with respect to different photon helicities. In spite of the lack of molecular chirality, a handedness may be induced in the photon-molecule system by the experimental geometry, considering enantiomorphic arrangements of the vectors corresponding to molecular orientation, photon propagation and electron ejection [9].

The circular dichroism in photoelectron angular distributions (CDAD) corresponds to the difference in the photoionization cross sections, differential in the emission polar angle θ_e relative to the molecular axis [see Fig. 1(a)], for left and right circularly polarized light. The CDAD of molecular

*Present address: Institut für Chemie und Biochemie, Freie Universität Berlin, Takustrasse 3, 14195 Berlin, Germany.

†Corresponding author; sanjose@fisica.udea.edu.co; Present address: Departamento de Química, Módulo 13, Universidad Autónoma de Madrid, 28049 Madrid, Spain.

‡Present address: Laboratoire Aimé Cotton, CNRS, Batiment 505, F-91405 Orsay Cedex, France.

§Present address: Departamento de Química Física, Facultad de Ciencias Químicas (Unidad asociada CSIC), Universidad Complutense de Madrid, 28040 Madrid, Spain.

‖Present address: School of Chemistry, University of Nottingham, Nottingham NG7 2RD, United Kingdom.

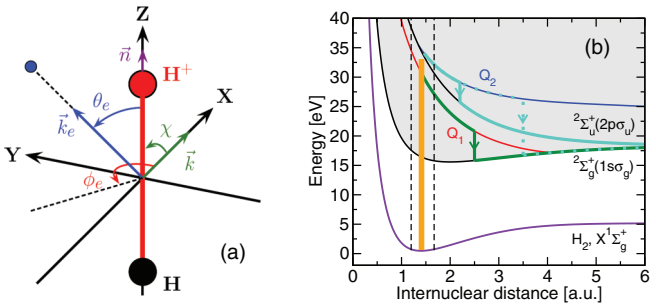

FIG. 1. (Color online) (a) Photoionization axis frame. The molecule is oriented along the Z axis. The light propagation direction is represented by the vector $\mathbf{k}$ along the X axis. The electron is ionized in the direction given by $\Omega_e = (\theta_e, \phi_e)$ and has a momentum vector $\mathbf{k}_e$. The proton is ejected in the upward direction ($\chi = 90°$) along the molecular axis $\mathbf{n}$. All results shown in the manuscript correspond to the YZ plane (i.e., $\chi = 90°$, $\phi_e = 90°$, or $\phi_e = 270°$). (b) Potential energy curves of H_2 and H_2^+. $X\,^1\Sigma_g^+$ denotes the ground electronic state of H_2 and $^2\Sigma_g^+(1s\sigma_g)$ and $^2\Sigma_u^+(2p\sigma_u)$, the ground and the first excited electronic states of H_2^+ (i.e., the first and the second ionization thresholds of H_2, respectively). A photon of 32.5 eV (orange vertical line) is absorbed by the H_2 molecule within the Franck-Condon region enclosed by dashed lines. The decay of the two lowest $^1\Sigma_u^+\ 1\mathcal{Q}_1$ and $^1\Pi_u\ 1\mathcal{Q}_2$ autoionizing states is indicated qualitatively with arrows.

photoelectrons from nonchiral oriented molecules was first investigated theoretically by Ritchie [10], who pointed out that such particular effects may appear due to interferences between the dipolar and higher-order terms in the multipole expansion of the radiation field. Cherepkov [11] predicted the existence of circular dichroism in the angular distributions of photoelectrons from oriented chiral molecules within the dipole approximation but assuming spin-orbit interaction. In a more detailed analysis [12,13], it was demonstrated that CDAD can also exist in oriented linear molecules even within the electric dipole approximation. Three major features were pointed out in the latter case: (i) CDAD in electron photoemission arises from the interference between degenerate continuum partial waves with m values differing by ± 1. (ii) CDAD vanishes if the triplet of vectors $(\mathbf{n}, \mathbf{k}_e, \mathbf{k})$ corresponding to the orientation of the molecular axis, the direction of the photoelectron momentum, and the direction of propagation of the circularly polarized light, respectively, are coplanar. (iii) For linear molecules with an inversion center, CDAD does not exist in the reflection plane perpendicular to the molecular axis. For other geometrical arrangements, such as the one adopted in the present work [see Fig. 1(a)] for dissociative ionization of H_2 and D_2, CDAD should be present.

Motivated by these predictions, Westphal *et al.* [14,15] reported the first experimental evidence of CDAD of photoelectrons ejected from oriented CO molecules, adsorbed on a crystal metal surface of Pd(111). Reid *et al.* [16] produced a first experiment in the gas phase with a complete description of the molecular photoionization, by measuring rotationally resolved CDAD with excited NO molecules. Completeness refers here to the determination of all complex dipolar transition matrix elements and their phases for each partial wave in the continuum. This kind of complete experiments has been extended nowadays to photoionization of molecules in the ground state, taking advantage of dissociative ionization and using multicoincidence detection methods like those mentioned above. By using these methods, CDAD has been observed [17–25] in molecular-frame photoelectron angular distributions (MFPADs) of oriented achiral molecules such as N_2, CO, NO, O_2, N_2O, H_2, and D_2, following direct or resonant inner- and valence-shell photoionization.

Multicoincidence detection methods are able to elucidate in which direction along the molecular axis the photoion is ejected. Thus, the experiment itself imposes boundary conditions for the ion (electron) localization after the prompt dissociation following the photoionization. This implies that the final total wave function is effectively projected onto stationary continuum states that localize one of the ions (or the remaining bound electron) in a given center. Assuming the geometry shown in Fig. 1, photoions may be released upwards or downwards, so that the delocalized nature of the remaining bound electron in H_2^+ (D_2^+) (a signature of the inversion symmetry) turns out to be now localized [$H(n\ell) + H^+$ or $H^+ + H(n\ell)$], i.e., the localized wave functions become $\varphi_{1s} = \frac{1}{\sqrt{2}}(\phi_{1\sigma_g} \pm \phi_{1\sigma_u})$. A discussion on this issue can be found in [26,27], in which MFPADs in dissociative photoionization of H_2 and D_2 are comprehensively analyzed for the case of linearly polarized light by using a time-independent perturbation theory.

One-photon absorption with circularly polarized light photoionizes H_2 (D_2) molecules from the ground state $X\,^1\Sigma_g^+$ to final continuum states $^1\Sigma_u^+$ and $^1\Pi_u$. For the photon energies considered in this work, only H_2^+ ionic thresholds $^2\Sigma_g^+(1s\sigma_g)$ and $^2\Sigma_u^+(2p\sigma_u)$ need to be considered [see Fig. 1(b)]. This implies that partial waves of the escaping photoelectron may have angular momentum ℓ odd (ungerade continuum orbitals for $1\sigma_g \varepsilon\ell$ channels) and ℓ' even (gerade continuum orbitals for $1\sigma_u \varepsilon\ell'$ channels) in both $^1\Sigma_u^+$ and $^1\Pi_u$ final symmetries. As we will see below, the origin of the observed CDAD and the presence of net circular dichroism CD after integration on the polar angle θ_e relies on an ℓ, ℓ' (even-odd) interference in the final-state partial waves with opposite inversion symmetry and m values differing by ± 1.

From our previous studies in H_2 [28] we have learned that CD effects occur at proton kinetic energies where DPI through both the $1s\sigma_g$ and $2p\sigma_u$ channels is possible. At these proton kinetic energies, CD is almost entirely determined by autoionization from the $\mathcal{Q}_1$ and $\mathcal{Q}_2$ doubly excited states of H_2. Although the autoionization lifetimes in H_2 and D_2 are identical, one can expect that CD is different, because, due to the different mass of the nuclei, the Franck Condon region in D_2 is narrower than in H_2, which implies differences in the photoexcitation process, and nuclear motion is slower, which modifies the dissociation dynamics.

In this work, we have theoretically and experimentally investigated CDAD of H_2 and D_2 and we report results in terms of photoelectron emission in the plane that contains the molecular axis and is perpendicular to the light propagation direction $\mathbf{k}$ for three photon energies: 20, 27, and 32.5 eV. This is an extension of our previous work reported in [28], where a more limited photon energy range was considered and resonant effects were investigated only for H_2. The present results show, in agreement with what was anticipated in Ref. [28]

for H_2, that for both molecular isotopes CD is possible due to the interference between direct photoionization and delayed autoionization from the $\mathcal{Q}_1$ and $\mathcal{Q}_2$ doubly excited states into ionic H_2^+ states of different inversion symmetry ($1s\sigma_g$ and $2p\sigma_u$). These interferences change dramatically as a function of the nuclear kinetic energy [29]. The present experimental results show the same qualitative behavior for H_2 and D_2 at the three photon energies, while the theory predicts that this behavior should be less similar at 32.5 eV (where autoionizations from $\mathcal{Q}_1$ and $\mathcal{Q}_2$ resonances are simultaneously relevant). The paper is organized as follows. In Sec. II, we introduce the basic formalism for CDAD and in Sec. III our time-dependent theory to obtain CDAD. Experimental and computational details are given in Secs. V and IV, respectively. In Sec. VI, we present our results and discussion. Atomic units are used throughout unless otherwise stated.

II. CIRCULAR DICHROISM FOR PHOTOEMISSION IN THE MOLECULAR FRAME

The molecular-frame photoelectron angular distribution $I(\chi,\theta_e,\phi_e)$ for the geometry shown in Fig. 1 takes a remarkably simple general form in the dipole approximation for incident circularly polarized light [20,30] [here $\mu_0 = 0$ is for linearly polarized light and, for instance, $\mu_0 = +1$ indicates left-handed circularly (LHC) polarized light of positive helicity $h = +1$]:

$$\begin{aligned} I_{\mu_0=\pm1,\chi,\phi_e}(\theta_e) = {} & F_{00}(\theta_e) - \tfrac{1}{2}F_{20}(\theta_e)P_2^0(\cos\chi) \\ & - \tfrac{1}{2}F_{21}(\theta_e)P_2^1(\cos\chi)\cos(\phi_e) \\ & - \tfrac{1}{2}F_{22}(\theta_e)P_2^2(\cos\chi)\cos(2\phi_e) \\ & \pm F_{11}(\theta_e)P_1^1(\cos\chi)\sin(\phi_e), \end{aligned} \tag{1}$$

where χ is the polar angle ($0 \leqslant \chi \leqslant \pi$) indicating the orientation of the molecular axis **n** with respect to the light propagation axis **k** and the set (θ_e,ϕ_e) indicates the direction of the electron emission vector $\mathbf{k}_e$ in the molecular frame, defined by the molecular axis and the light propagation axis.

In Eq. (1), the dependence on the azimuthal angle ϕ_e and the molecular orientation angle χ is factorized in terms of simple trigonometric functions and associated Legendre polynomials P_{LN}, respectively, so that complete dynamical information about the dissociative photoionization reaction is fully described by the five $F_{LN}(\theta_e)$ functions [31]. These functions can be determined experimentally by performing a Legendre-Fourier analysis in (χ, ϕ_e) of the MFPAD $I(\chi,\theta_e,\phi_e)$, using expression (1). The F_{LN} functions depend on the polar angle θ_e and the total energy (electronic and nuclear) of the final continuum state. To emphasize the geometrical aspect of these functions, the latter dependence has been omitted in the notation. When photoionization is fast in comparison with dissociation of the molecular ion [20], variations with total energy are entirely due to variations in the photoelectron energy, since the nuclei barely move and therefore their kinetic energy remains nearly constant [20]. However, when, as in the present study, both ionization and dissociation occur on a comparable time scale, the energy in the final state is shared between electrons and nuclei, and consequently the $F_{LN}(\theta_e)$ functions do vary with the photoion kinetic energy [28,32]. We will use this dependence upon θ_e and the photoion kinetic energy to present and discuss our results. In particular, the F_{21} function gives access to the absolute value of the relative phase between the amplitudes for parallel (${}^1\Sigma_g^+ \rightarrow {}^1\Sigma_u^+$) and perpendicular (${}^1\Sigma_g^+ \rightarrow {}^1\Pi_u$) dipole transitions, whereas F_{11} (accessed only by using circularly polarized light) provides the sign of this relative phase and determines the presence of circular dichroism. Once these five functions are extracted experimentally or calculated, MFPADs for any orientation χ of the molecular axis can be fully reconstructed.

The observation of CDAD in the molecular frame is largest for electron scattering in a plane YZ perpendicular to the light propagation axis ($\phi_e = 90^\circ$ or 270°) and containing the molecular axis ($\chi = 90^\circ$), due to the $\sin\phi_e$ dependence in Eq. (1). For the geometry adopted in this work, $\chi = 90^\circ$, Eq. (1) reduces to

$$\begin{aligned} I_{\mu_0=\pm1,\chi=90,\phi_e}(\theta_e) = {} & F_{00}(\theta_e) + \tfrac{1}{4}F_{20}(\theta_e) - \tfrac{3}{2}F_{22}(\theta_e)\cos(2\phi_e) \\ & \pm F_{11}(\theta_e)\sin(\phi_e), \end{aligned} \tag{2}$$

and only four F_{LN} functions are needed. In this YZ plane, CDAD is characterized as the relative variation of the MFPAD $I(\chi = 90^\circ,\theta_e,\phi_e = 90^\circ)$ [or $I(\chi = 90^\circ,\theta_e,\phi_e = 270^\circ)$] when the helicity of the light is changed from $h = +1$ (LHC polarized) to $h = -1$ (RHC polarized). In fact, CDAD can be defined in two equivalent forms, and expressed straightforwardly in terms of the F_{LN} functions:

$$\begin{aligned} \mathrm{CDAD}_{\chi=90,\phi_e=90}(\theta_e) &= \frac{I_{+1,90,90} - I_{-1,90,90}}{I_{+1,90,90} + I_{-1,90,90}} \\ &= \mathrm{CDAD}_{\chi=90,h=+1}(\theta_e) = \frac{I_{+1,90,90} - I_{+1,90,270}}{I_{+1,90,90} + I_{+1,90,270}} \\ &= \frac{2F_{11}}{2F_{00} + \frac{1}{2}F_{20} + 3F_{22}}. \end{aligned} \tag{3}$$

Accordingly, CDAD is driven by the function F_{11} and takes values in the interval $[-1,+1]$. In most experiments performed so far on homonuclear diatomic molecules [18,22–24], CDAD exhibits an antisymmetric behavior with respect to the polar electron emission angle θ_e in the plane perpendicular to the light propagation. In this case, the net circular dichroism CD, defined by integrating over the polar angle, i.e.,

$$\mathrm{CD} = \frac{\int \sin\theta_e d\theta_e (I_{+1,90,90} - I_{-1,90,90})}{\int \sin\theta_e d\theta_e (I_{+1,90,90} + I_{-1,90,90})} \tag{4}$$

vanishes identically. However, we have recently found [28] that CDAD in resonant DPI of H_2 (for impact photon energies in the range 30–35 eV) may strongly depart from the expected antisymmetry in θ_e in specific regions of the ion kinetic-energy release spectrum, and thus the θ_e-integrated CD does not vanish, but shows instead a richer structure attributed to delayed autoionization of $\mathcal{Q}_n$ molecular resonances into channels with different inversion symmetry.

III. THEORETICAL METHOD

MFPADs obtained through DPI of simple molecules can be evaluated by using time-independent theories. For instance, the multichannel Schwinger configuration-interaction method

(MC-SCI) of Lucchese and co-workers [33–35] has been shown to provide accurate predictions of molecular-frame photoemission observables measured for a series of molecular targets [20–22,30,31]. Density functional theory (DFT) calculations have also been conducted and predict richly structured measured angular distributions from fixed-in-space small polyatomic molecules [36], with recent developments involving time-dependent DFT [37]. All these calculations were performed within the fixed-nuclei approximation. However, the study of resonant DPI, when autoionization and dissociation occur on a comparable time scale, requires a more sophisticated theory since the nuclei have time to move before the electron is ejected. This can be done only by using a full quantum-mechanical treatment of both the electronic and nuclear motions [38]. This time-independent theory along with Dill's formulas [2] have been used to compute MFPADs in H_2 and D_2 for linearly polarized light [27] as well as for circularly polarized light [23,39]. Here we use instead a recent extension of this methodology to the time domain [40], which allows for the temporal scrutiny of the resonant photodynamics involved in CDAD. The adiabatic and the dipolar approximations are assumed. The axial recoil approximation [41] is also invoked since superexcited states in H_2 dissociate faster than the rotational period of the molecule. In practice, this means that the set $(\mathbf{V}_{H^+},\mathbf{V}_e,\hat{\boldsymbol{\epsilon}}_p)$ in the vector correlation method are connected with the triplet of vectors $(\mathbf{n},\mathbf{k}_e,\mathbf{k})$, and corrections due to rotational motion are neglected.

Our method [40] is based on the solution of the time-dependent Schrödinger equation (TDSE):

$$[\mathcal{H}^0(\mathbf{r},R)+V^{\mu_0}(t)-i\,\partial_t]\Phi(\mathbf{r},R,t)=0, \tag{5}$$

where $\mathbf{r}$ labels the electronic coordinates $\mathbf{r}_1$ and $\mathbf{r}_2$, R is the internuclear distance, and $\mathcal{H}^0$ is the H_2 field-free nonrelativistic Hamiltonian neglecting the mass polarization term

$$\mathcal{H}^0(\mathbf{r},R)=T(R)+\mathcal{H}_{el}(\mathbf{r},R). \tag{6}$$

Here $T(R)=-\nabla_R^2/2\mu$, $\mathcal{H}_{el}$ is the electronic Hamiltonian, and V^{μ_0} is the laser-molecule interaction potential in the velocity gauge

$$V^{\mu_0}(t)=(\mathbf{p}_1+\mathbf{p}_2)\cdot\mathbf{A}^{\mu_0}(t), \tag{7}$$

where $\mathbf{p}_i$ is the linear momentum operator for the electron i and $\mathbf{A}^{\mu_0}$ is the vector potential of the radiation field with polarization μ_0. The dipolar operator is commonly referred to the laboratory frame but one can make use of the Wigner rotation matrices to express the operator in the molecular frame [2]. Within the dipole approximation, for circularly polarized light defined by the parameter μ_0 and considering the geometry of Fig. 1, we choose the vector potential to be different from zero in the time interval $[0,T]$ according to the formula

$$\mathbf{A}^{\mu_0}(t)=A_0\sin^2\left(\frac{\pi}{T}t\right)\begin{pmatrix}0\\ \mu_0\cos\left[\omega\left(t-\frac{T}{2}\right)\right]\\ \sin\left[\omega\left(t-\frac{T}{2}\right)\right]\end{pmatrix}, \tag{8}$$

where A_0 is the vector potential amplitude, which is related to the laser peak intensity by $A_0/\omega=[I\ (\mathrm{W/cm^2})/3.5095\times 10^{16}]^{1/2}$.

The time-dependent wave function $\Phi(\mathbf{r},R,t)$ is expanded in a basis of fully correlated adiabatic Born-Oppenheimer (BO) vibronic stationary states of energy W_k, which include the bound states, the resonant doubly excited states, and the nonresonant continuum states of H_2 [40]:

$$\begin{aligned}\Phi(\mathbf{r},R,t)&=C_{g\nu_g}(t)\phi_g(\mathbf{r},R)\chi_{\nu_g}(R)e^{-iW_{g\nu_g}t}\\&+\sum_r\sum_{\nu_r}C_{r\nu_r}(t)\phi_r(\mathbf{r},R)\chi_{\nu_r}(R)e^{-iW_{r\nu_r}t}\\&+\sum_{\alpha\ell m}\int d\varepsilon\sum_{\nu_\alpha}C^{\varepsilon\ell m}_{\alpha\nu_\alpha}(t)\psi^{\varepsilon\ell m}_{\alpha}(\mathbf{r},R)\chi_{\nu_\alpha}(R)e^{-iW_{\alpha\nu_\alpha}t},\end{aligned} \tag{9}$$

where ϕ_g, ϕ_r, and $\psi^{\varepsilon\ell m}_\alpha$ represent the ground, doubly excited, and continuum electronic states of H_2 (or D_2), respectively. Here, α represents the full set of quantum numbers for the electronic state of the residual molecular ion H_2^+ (or D_2^+) with BO energy $E_\alpha(R)$ and the indices ε, ℓ, and m correspond, respectively, to the kinetic energy, angular momentum, and the Z component of the angular momentum of the ejected electron.

The vibronic states in Eq. (9) result from the solution of the following eigenvalue equations [40]: (i) for the electronic motion

$$[\mathcal{H}_{el}-\mathcal{E}_g(R)]\phi_g=0, \tag{10}$$

$$[\mathcal{Q}\mathcal{H}_{el}\mathcal{Q}-\mathcal{E}_r(R)]\phi_r=0, \tag{11}$$

$$[\mathcal{P}\mathcal{H}_{el}\mathcal{P}-\mathcal{E}_\alpha(R)]\psi^{\varepsilon\ell m}_\alpha=0, \tag{12}$$

where $\mathcal{P}$ and $\mathcal{Q}=1-\mathcal{P}$ are Feshbach projection operators that project onto the nonresonant and resonant parts of the continuum wave function, respectively, and (ii) for the nuclear motion

$$[T(R)+\mathcal{E}_g(R)-W_{g,\nu_g}]\chi_{\nu_g}=0, \tag{13}$$

$$[T(R)+\mathcal{E}_r(R)-W_{r,\nu_r}]\chi_{\nu_r}=0, \tag{14}$$

$$[T(R)+\mathcal{E}_\alpha(R)+\varepsilon-W_{\alpha,\nu_\alpha}]\chi_{\nu_\alpha}=0, \tag{15}$$

where $W_{x\nu_x}$ refers to the total vibronic energy.

The electronic wave functions ϕ_r and $\psi^{\varepsilon\ell m}_\alpha$ are not eigenfunctions of the electronic Hamiltonian, which can be written as a sum of projected operators $\mathcal{H}_{el}=\mathcal{Q}\mathcal{H}_{el}\mathcal{Q}+\mathcal{P}\mathcal{H}_{el}\mathcal{P}+\mathcal{Q}\mathcal{H}_{el}\mathcal{P}+\mathcal{P}\mathcal{H}_{el}\mathcal{Q}$. The $\mathcal{Q}\mathcal{H}_{el}\mathcal{P}$ term describes the interaction between the $\mathcal{Q}$ and $\mathcal{P}$ subspaces, which is responsible for the autoionizing decay of the doubly excited states into the continuum. Thus, by introducing the ansatz (9) into the TDSE (5) and projecting onto the basis of stationary vibronic states, one arrives at a set of coupled linear differential equations in which these couplings, in addition to the dipole-induced ones, explicitly appear [40],

$$\begin{aligned}i\frac{d}{dt}&\begin{pmatrix}C_{g\nu_g}\\ C_{r\nu_r}\\ C^{\varepsilon\ell m}_{\alpha\nu_\alpha}\end{pmatrix}\\&=\begin{pmatrix}0 & A(t)V^{r\nu_r}_{g\nu_g} & A(t)V^{\alpha\nu_\alpha\varepsilon\ell m}_{g\nu_g}\\ A(t)V^{g\nu_g}_{r\nu_r} & 0 & \mathcal{Q}\mathcal{H}\mathcal{P}^{\alpha\nu_\alpha\varepsilon\ell m}_{r\nu_r}\\ A(t)V^{g\nu_g}_{\alpha\nu_\alpha\varepsilon\ell m} & \mathcal{P}\mathcal{H}\mathcal{Q}^{r\nu_r}_{\alpha\nu_\alpha\varepsilon\ell m} & 0\end{pmatrix}\begin{pmatrix}C_{g\nu_g}\\ C_{r\nu_r}\\ C^{\varepsilon\ell m}_{\alpha\nu_\alpha}\end{pmatrix},\end{aligned} \tag{16}$$

where each matrix term represents a matrix block and we have neglected nonadiabatic electrostatic couplings. This system of equations must be integrated for $t \geqslant T$. This time must be larger than the lifetime of the $\mathcal{Q}_{1,2}$ resonant states to allow for their complete decay [40]. In the velocity gauge, the operator $\mathbf{p}_{j\mu_0} = -i\nabla_{j\mu_0}$ is $-i\partial/\partial z_j$ for $\mu_0 = 0$ (linear polarization along the molecular axis) and $-i(\mp\partial/\partial z_j \pm i\partial/\partial y_j)/\sqrt{2}$ for $\mu_0 = \pm 1$ (circular polarization with components in the YZ plane). Given that the light propagation vector lies on the X axis (see Fig. 1) one needs to consider only the Y and Z components of the dipolar operator. In this work we will consider only very weak intensities, so that the population of the initial state $X\,^1\Sigma_g^+$ remains very close to 1 for all times and multiphoton absorption is negligible compared to one-photon absorption. Thus, in practice, we can consider two sets of coupled equations, the first one for final states $^1\Sigma_u^+$ (parallel transitions to states with $\Lambda = 0$ and $m = 0$) and the second one for final states $^1\Pi_u$ (perpendicular transitions to states with $\Lambda = 1$ and $m = \pm 1$). After propagating both sets separately, the asymptotic amplitudes are collected and then added coherently in the differential cross sections as explained below.

The asymptotic wave function that describes an ejected electron in channel α satisfying incoming wave boundary conditions admits a partial-wave decomposition [2]:

$$\Psi_\alpha^{(-)}(\mathbf{r},R,t) = \sum_{\ell m} i^\ell e^{-i\sigma_\ell(\varepsilon)} \mathcal{Y}_\ell^{m*}(\theta_e,\phi_e) \times \psi_\alpha^{\varepsilon\ell m}(\mathbf{r},R)\chi_{v_\alpha}(R)e^{-iW_{\alpha v_\alpha}t}, \quad (17)$$

where $\sigma_\ell(\varepsilon) = \arg\Gamma(\ell + 1 - i/\sqrt{2\varepsilon})$ is the Coulomb phase shift. As mentioned in the Introduction, vector correlation methods are capable of detecting the momentum and direction of all ejected charged particles, and specifically of elucidating in which direction along the internuclear distance axis the proton escaped. With reference to Fig. 1, protons may be released upwards (U) or downwards (D) and, consequently, a combination of the partial-wave expansions for the $1s\sigma_g$ and $2p\sigma_u$ channels must be performed to fulfill the specific asymptotic condition [26]

$$\Psi_{U,D}^{(-)} = \frac{1}{\sqrt{2}}\left[\Psi_{1s\sigma_g}^{(-)} \pm \Psi_{2p\sigma_u}^{(-)}\right], \quad (18)$$

which implies that final transition amplitudes $(C_{1s\sigma_g v}^{\varepsilon\ell m}, C_{2p\sigma_u v}^{\varepsilon\ell m})$ are added for the U case and substracted for the D case.

Molecular-frame photoelectron angular distributions or, equivalently, photoionization probabilities differential in proton energy ($E_{H^+} = W_{\alpha,v_\alpha} - W_\infty$, where W_∞ is the energy of a H atom infinitely separated from H^+) and in the solid angle of the ionized electron, can be evaluated following Dill's procedure [2], for any arbitrary polarization μ_0, replacing the dipolar transition matrix elements by the asymptotic transition amplitudes obtained after integrating the TDSE:[1]

$$\frac{d^3P^{\mu_0}}{d\Omega_n dE_{H^+} d\Omega_e} = \int d\varepsilon \sum_{\alpha_a\alpha_b}\sum_{\mu_a\mu_b}\sum_{\ell_a m_a}\sum_{\ell_b m_b} i^{(\ell_a-\ell_b)} e^{i[\sigma_{\ell_b}(\varepsilon)-\sigma_{\ell_a}(\varepsilon)]}(-1)^{m_b+\mu_a-\mu_0}\left(C_{\alpha_a v}^{\varepsilon\ell_a m_a\mu_a}\right)^*\left(C_{\alpha_b v}^{\varepsilon\ell_b m_b\mu_b}\right) \times \sum_{L_e}\sqrt{\frac{(2\ell_a+1)(2\ell_b+1)}{2L_e+1}}\langle\ell_a\ell_b 00|L_e 0\rangle\langle\ell_a\ell_b - m_a m_b|L_e M_e\rangle\mathcal{Y}_{L_e}^{M_e*}(\theta_e,\phi_e) \times \sum_L\sqrt{\frac{1}{2L+1}}\langle 11-\mu_a\mu_b|LN\rangle\langle 11-\mu_0\mu_0|L0\rangle\mathcal{Y}_L^N(\theta_n,\phi_n), \quad (19)$$

with

$$\mu_{a,b} = 0,\pm 1, \quad N = -\mu_a + \mu_b, \quad M_e = -m_a + m_b,$$
$$\ell_a + \ell_b \geqslant L_e \geqslant |\ell_a - \ell_b| \quad \text{and} \quad 0 \leqslant L \leqslant 2.$$

In this equation, $\Omega_e = (\theta_e,\phi_e)$ is the solid angle for the photoelectron emission direction, $\chi \equiv \Omega_n = (\theta_n,\phi_n)$ (see Fig. 1), $\langle j_1 j_2 m_1 m_2|JM\rangle$ denotes a Clebsch-Gordan coefficient, and $C_{\alpha_{a,b}v_{\alpha_{a,b}}}^{\varepsilon\ell_{a,b}m_{a,b}\mu_{a,b}}$ is the transition amplitude to a continuum vibronic state for a given value of $\mu_{a,b}$ and for the given channel $\alpha_{a,b} = U$ or D as defined in Eq. (18). Note that in Eq. (19) the first summation over α_a and α_b runs over the two ionization channels corresponding to the $1s\sigma_g$ and $2p\sigma_u$ states, for both the parallel ($^1\Sigma_g \to {}^1\Sigma_u$) and the perpendicular ($^1\Sigma_g \to {}^1\Pi_u$) transitions. The indices ℓ_a and ℓ_b represent the angular momenta of the ejected electron for each channel and final symmetry.

As shown in [31], Eq. (19) for MFPADs is formally and computationally equivalent to Eq. (1), expressed in terms of F_{LN} functions and simple trigonometric functions. To see the connection, the F_{LN} functions can be partial-wave expanded in terms of Legendre polynomials and transition amplitudes as a function of the total vibronic energy $W_{\alpha v_\alpha}$, or equivalently, the proton kinetic energy E_{H^+}:

$$F_{LN}(E_{H^+},\theta_e) = \sum_{L_e=|\ell_a-\ell_b|}^{\ell_a+\ell_b} D_{L_e LN}^{\mu_0}(E_{H^+})P_{L_e}^N(\cos\theta_e), \quad (20)$$

[1]Note that, in Eq. (1) of Ref. [27], a factor $4\pi^2\omega/c$ was introduced, so that the square of the transition amplitude directly leads to cross sections in the framework of time-independent perturbation theory. In the present work, approximate cross sections may be retrieved by multiplying the asymptotic transition probabilities by a factor $3\omega/8TI$ [40].

where

$$
\begin{aligned}
&D^{\mu_0}_{L_e LN}(E_{\mathrm{H}^+}) \\
&= \frac{(-1)^N(-i)^{\delta_{L,1}\delta_{N,1}}}{1+\delta_{N,0}} i^{(\ell_a-\ell_b)} \\
&\times \sum_{\alpha_a\alpha_b}\sum_{\mu_a\mu_b}\sum_{\ell_a m_a}\sum_{\ell_b m_b}(-1)^{m_b+\mu_a-\mu_0} \\
&\times \sqrt{\frac{(2\ell_a+1)(2\ell_b+1)(L_e-N)!(L-N)!}{(L_e+N)!(L+N)!}} \\
&\times \langle \ell_a \ell_b 00|L_e 0\rangle \langle \ell_a \ell_b m_a - m_b|L_e - N\rangle \\
&\times \langle 11-\mu_a\mu_b|LN\rangle \langle 11-\mu_0\mu_0|L0\rangle \\
&\times \int d\varepsilon \left(C^{\varepsilon \ell_a m_a \mu_a}_{\alpha_a \nu}\right)^* \left(C^{\varepsilon \ell_b m_b \mu_b}_{\alpha_b \nu}\right) e^{i[\sigma_{\ell_b}(\varepsilon)-\sigma_{\ell_a}(\varepsilon)]}. \qquad (21)
\end{aligned}
$$

The F_{LN} functions can be accessed experimentally as a function of the proton kinetic energy, so that a direct comparison between theory and experimental results for MFPADs is already feasible at this partial-wave level, providing the strongest test of theory and experiment, since it is done at the level of transition amplitudes and their relative partial-wave phase shifts.

IV. COMPUTATIONAL DETAILS

A detailed description of this method can be found in [38,40,42]. Briefly, a standard configuration-interaction (CI) method is used to obtain the H_2 ground state $X\,^1\Sigma_g^+$ and bound excited state, whereas a truncated CI method compatible with the Feshbach formalism is used to obtain the resonant states $\mathcal{Q}_{1,2}\,^1\Sigma_u^+$ and $\mathcal{Q}_{1,2}\,^1\Pi_u$. The CI method uses H_2^+ orbitals expanded in one center, in terms of a basis set consisting of 180 B splines of order $k=8$, including angular momenta from $\ell=0$ up to $\ell=16$ enclosed in an electronic box of size 60 a.u. For a more detailed description of B splines and their applications in atomic and molecular physics, see [42]. Nonresonant electronic continuum states $\psi_\alpha^{\varepsilon \ell m}$ are evaluated by using an $\mathcal{L}^2$ close-coupling approach. The uncoupled continuum states (UCSs) that enter in this formalism are built up as antisymmetrized configurations of the type $[n\ell\lambda_\pi(\mathbf{r}_1), n\lambda_\pi^{(\ell)}(\mathbf{r}_2)]$, where $n\ell\lambda_\pi$ corresponds to a $H_2{}^+$ target state and $n\lambda_\pi^{(\ell)}$ is a $H_2{}^+$ orbital that represents the ionizing electron within the subspace of angular momentum ℓ and parity π. For instance, the configurations for the four continua used in this work have the following forms:

(a) two continua of symmetry $^1\Sigma_u^+$ built up with configurations $1s\sigma_g n\sigma_u^{(\ell)}$ ($n=1,75$) for channels with $\ell=1$, 3, 5, and 7, and $2p\sigma_u n\sigma_g^{(\ell)}$ ($n=1,75$) for $\ell=0$, 2, 4, and 6;

(b) two continua of symmetry $^1\Pi_u$ built up with configurations $1s\sigma_g n\pi_u^{(\ell)}$ ($n=1,75$) for $\ell=1$, 3, 5, and 7, and $2p\sigma_u n\pi_g^{(\ell)}$ ($n=1,75$) for $\ell=2$, 4, 6, and 8.

These UCSs are then energy normalized and interchannel coupling between the different degenerate ℓ channels is introduced by solving the Lippman-Schwinger equation [38,42,43]. The vibrational wave functions χ_{ν_g}, χ_{ν_r}, and χ_{ν_α} are also expanded in terms of a B-spline basis set, using 240 B splines of order $k=8$ inside a box of $R_{\max}=12$ a.u. For the time-dependent solution, we use a sixth-order Runge-Kutta integrator to solve a system of equations that reaches dimensions up to 30 000 vibronic states. Experimental results on circular dichroism have been obtained with synchrotron radiation. This condition may be achieved in a time-dependent methodology by propagating the TDSE using laser pulses with relatively low intensities and long duration. Such perturbative stationary conditions are met with a pulse duration $T=10$ fs and a laser peak intensity of $I=10^{12}$ W/cm^2. Transition amplitudes $C^{\varepsilon \ell m}_{\alpha \nu_\alpha}$ ($t>T$) (which also carry the short-range phase shift) for $^1\Sigma_u^+$ and $^1\Pi_u$ final states are collected for all ℓ partial waves in a discretized set of continuum energies ε and then inserted in Eq. (19) or (21).

V. EXPERIMENTAL DETAILS

A description of the experimental setup used in applying the vector correlation (VC) method for the most recent measurements of MFPADs in D_2 has already been outlined in [44]. It allows measuring in coincidence the ejection velocity vectors of photoelectrons and photoions emitted in the same DPI event for molecules in the gas phase subject to synchrotron radiation. A double electron-ion velocity spectrometer [5] combines time-of-flight- (TOF-) resolved ion-electron coincidence detection and imaging techniques with position-sensitive detection. A collimated beam of H_2 (D_2) molecules emerges from the supersonic molecular jet SAPHIRS [45] and the circularly polarized light is provided by the VUV beamline DESIRS at the third-generation synchrotron radiation facility SOLEIL, operated in the eight-bunch mode with a period $T=147$ ns and a pulse width limited to $\Delta t=50$ ps. The circular polarization rate s_3/s_0 of the light, where (s_0,s_1,s_2,s_3) are the Stokes parameters, was higher than 95%. The two beams intersect at right angles in the interaction region located at the center of the spectrometer.

Electrons and ions resulting from DPI are extracted from the interaction region by a dc uniform electric field (from 15 V/cm for photons of $\hbar\omega=19$ eV up to 150 V/cm for photon energies of $\hbar\omega=32.5$ eV), then focused with two electrostatic lenses ensuring a 4π collection of both particles in the energy region of interest, and finally collected by the two-delay line position-sensitive detectors (PSDs) DLD40 RoentDek. The three components of the velocity in $(\mathbf{V}_{\mathrm{H}^+},\mathbf{V}_e)$ for each coincident DPI event are deduced from the impact positions of the particles at the PSDs and their TOF. The space focusing induced by the electrostatic lenses reduces the influence of the finite dimensions of the interaction region on the spatial resolution, while the global bending of the ion and/or electron trajectories preserving the time-of-flight information enables us to achieve an efficient collection of the emitted particles for a reduced magnitude of the extraction field. This property minimizes the influence of the finite temporal resolution, of the order of 150 ps in these experiments, mostly influencing the resolution of the electron versus velocity component parallel to the extraction field. The instrumental widths are implemented in a Monte Carlo simulation of the charged particle trajectories which enables us to convolute the theoretical results with the apparatus function as presented below. Since the ion-fragment energy resolution is estimated at about 0.5 eV for extraction fields of the order of 100 V/cm, the evolution of the MFPADs as a function of

the proton kinetic energy (KE) will be presented for selection of the coincident events in bands of corresponding KE width.

The VC method allows for the construction of ion-electron kinetic-energy correlation diagrams (KECDs), which corresponds to a two-dimensional (2D) histogram of the (H^+, e^-) coincident events, deduced from the analysis of the moduli of the ($\mathbf{V}_{H^+}$,$\mathbf{V}_e$) vectors. This probability distribution is represented as a function of the electron energy and the photoion kinetic energy. A detailed analysis of the events in these KECDs for H_2 and D_2 DPI has been discussed elsewhere [44,46]. By integrating the KECDs over the electron energy one obtains the DPI cross section as a function of the photoion KE.

The F_{LN} functions in Eq. (1) for each process appearing in the KECD diagrams with energies (E_{H^+}, E_{e^-}) are extracted from all the coincident events (H^+, e^-) recorded with a 4π collection by the VC method, by performing a Legendre-Fourier analysis (with a three-angle fit) of the directly measured MFPAD $I(\chi,\theta_e,\phi_e)$ distribution. Therefore MFPADs can be discriminated for any photoion KE or electron energy [32].

VI. RESULTS

We present results for MFPADs, CDAD, and total CD in DPI of both H_2 and D_2 molecules, excited by three different photon energies, which represent distinct physical situations in terms of the role that autoionizing processes play in the photodynamics: 20 eV for H_2 (and 19 eV for D_2), 27 eV, and 32.5 eV. Figures 2 and 3 show the dissociative ionization probability components, which correspond (up to a scale factor 2π) to the (θ_e,ϕ_e)-integrated quantity $F_{00}+0.25F_{20}$; the insets represent polar plots of the MFPADs resulting from Eq. (2) or Eq. (19) for orientational molecular geometry $\chi=90^\circ$ and $\phi_e=90^\circ$ (left side) and $\phi_e=270^\circ$ (right side), as a function of $H^+(D^+)$ KE. At photon energies around 20 eV, the dominant process is direct nonresonant dissociative photoionization into the dissociative part of the $H_2{}^+\,{}^2\Sigma_g^+(1s\sigma_g)$ channel (see Fig. 1) for both final symmetries $^1\Sigma_u^+$ and $^1\Pi_u$ (in the following, symbols within parentheses indicate the ionization channel $nl\lambda_{g,u}$ and the symmetry of the final electronic state $^{2S+1}\Lambda_{g,u}^{\pm}$):

$$H_2+\hbar\omega\rightarrow H+H^+ +e^-[1s\sigma_g,{}^1\Sigma_u^+\,({}^1\Pi_u)]. \qquad (22)$$

This process is relevant only at very low $H^+(D^+)$ kinetic energies, which is a consequence of the rapid decrease of the Franck-Condon overlap between the initial vibrational state of the H_2 (D_2) and the vibrational states corresponding to the dissociative continuum of $H_2{}^+(D_2{}^+)$. At this photon energy, when linear polarization is used, the photoelectron emission is preferentially produced in the form of a p wave, indicating that the first partial wave for the ejected electron [$\sigma_u^{(\ell_a=1)}$ ($\pi_u^{(\ell_b=1)}$) for $^1\Sigma_u^+$ ($^1\Pi_u$) final symmetries, respectively] dominates [27]. Thus, according to Eqs. (20) and (21), the dominant contributions to the MFPADs come from $L_e=0$, 1, and 2. When using left circularly polarized light with the polarization vector rotating in the YZ plane, contributions from the molecular orientations parallel ($^1\Sigma_u^+$) and perpendicular ($^1\Pi_u$) to the polarization axis are added coherently. Available experimental results in D_2 for the DPI probability and the MFPADs are in very good agreement with the calculations.

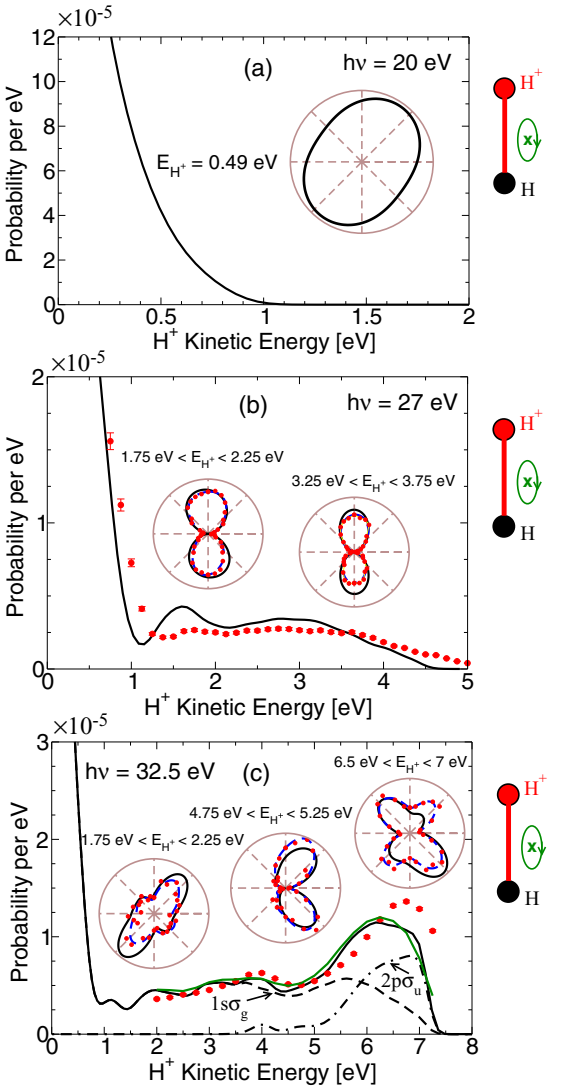

FIG. 2. (Color online) Dissociative ionization probability in H_2 as a function of the proton kinetic energy for left-handed circularly polarized light for three photon energies: (a) $\omega=20$ eV, (b) $\omega=27$ eV, and (c) $\omega=32.5$ eV. The probability corresponds to the geometry displayed in Fig. 1 and it is equal to the quantity $F_{00}+0.25F_{20}$ after integrating Eq. (2) over θ_e and ϕ_e. Experiment and theory are normalized on the θ_e-integrated F_{00} summed in a broad KE range chosen for each photon energy. Red circles, experimental results; black solid line, theoretical results; green solid line, theoretical results convoluted with the instrumental resolution; black dashed line, dissociative ionization probability associated with the $1s\sigma_g$ ionization channel; black dash-dotted line, probability associated with the $2p\sigma_u$ channel. Insets: Polar plots of the MFPADs in the YZ plane at fixed proton kinetic energies averaged within the energy intervals indicated in the figure. Same notation as for the probabilities plus a blue dashed line indicating a fitting to the experimental results.

For a photon energy of 27 eV the autoionization process (AI) through $\mathcal{Q}_1$ doubly excited states is now an open channel (a process indicated qualitatively in Fig. 1), i.e.,

$$H_2+\hbar\omega\rightarrow H_2^{**}(\mathcal{Q}_1\,{}^1\Sigma_u^+)\rightarrow H+H^+ +e^-(1s\sigma_g,{}^1\Sigma_u^+), \qquad (23)$$

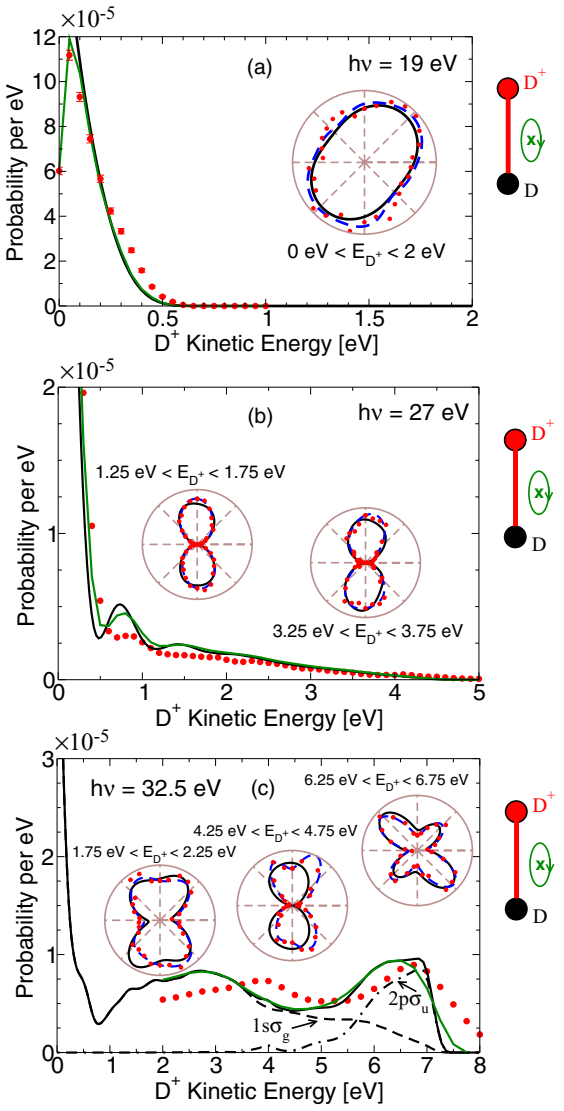

FIG. 3. (Color online) As fig. 2 but with D_2.

which adds up to the direct ionization process of Eq. (22). The contribution of $\mathcal{Q}_1$ resonances of $^1\Pi_u$ symmetry is almost negligible in comparison with those of $^1\Sigma_u^+$ symmetry and direct ionization to $2p\sigma_u$ is nearly a closed channel. The kinetic-energy distributions of the DPI yields shown in Figs. 2(b) and 3(b) for H_2 and D_2, respectively, now show structures beyond 1 eV attributed to interferences between DPI and AI channels. These structures are expected to be more pronounced in H_2 than in D_2, since the effective Frank-Condon region in D_2 is narrower than in H_2 and fewer doubly excited states are populated. Experimental results for D_2 [Fig. 3(b)] show a pattern of smooth oscillations above the direct dissociative ionization contribution (KE $>$ 0.5 eV) in agreement with our theoretical results. Concerning MFPADs at 27 eV, they show a dominant p-like orbital shape. This is because the dominant contribution to autoionization into the H_2^+ $(1s\sigma_g)$ channel comes from the $1\mathcal{Q}_1$ $^1\Sigma_u^+$ doubly excited state, which mainly decays into a $\sigma_u^{(\ell=1)}$ partial wave. This p-wave behavior is quite robust in the whole KE spectrum due to the rather small contribution of DPI and AI involving $1s\sigma_g$ and $2p\sigma_u$ ionization channels of $^1\Pi_u$ symmetry.

For a photon energy of 32.5 eV [Figs. 2(c) and 3(c)], both photoionization yields and MFPADs are much more complex due to the increasing number of channels involved. In addition to the processes described by Eq. (22) and (23) (the latter now contributing to the ionization signal up to 7.5 eV), new reactions add up due to DPI into the open $2p\sigma_u$ ionization channel and AI from the $\mathcal{Q}_2$ $^1\Pi_u$ doubly excited states to the $1s\sigma_g$ and $2p\sigma_u$ ionization channels (see Fig. 1), i.e.,

$$H_2 + \hbar\omega \rightarrow H + H^+ + e^-[2p\sigma_u, {}^1\Sigma_u^+ ({}^1\Pi_u)] \qquad (24)$$

and

$$\begin{aligned} H_2 + \hbar\omega &\rightarrow H_2^{**}(\mathcal{Q}_2\ {}^1\Pi_u) \\ &\rightarrow H + H^+ + e^-[1s\sigma_g(2p\sigma_u), {}^1\Pi_u]. \end{aligned} \qquad (25)$$

Processes leading to ionization in the $1s\sigma_g$ channel contribute to different regions of the KE spectrum. DPI of Eq. (22) is significant only at low fragment kinetic energies (0–1 eV), the AI process (23) contributes to all kinetic energies above 1 eV, whereas the decay of the $\mathcal{Q}_2$ $^1\Pi_u$ resonances contributes at intermediate energies ($E_{\rm kin} \sim$ 1–5 eV). In contrast, processes involving the second ionization channel $2p\sigma_u$, (24) and (25), contribute from the intermediate- to the high-energy region ($E_{\rm kin} \sim$ 4–7.5 eV). Although not shown explicitly in Figs. 2 and 3, for the $1s\sigma_g$ ionization channel, the contribution from the $^1\Sigma_u^+$ symmetry is larger than from the $^1\Pi_u$ one, while the opposite occurs for the $2p\sigma_u$ channel.

Pure parallel transitions to $^1\Sigma_u^+$ final states or perpendicular ones to $^1\Pi_u$ final states induced by linearly polarized light lead to MFPADs that should preserve g-u inversion symmetry, unless, as explained in [26], $1s\sigma_g$ and $2p\sigma_u$ ionization channels contribute significantly in the same ion kinetic-energy region. With circularly polarized light, $^1\Sigma_u^+$ and $^1\Pi_u$ channels are entangled, which can break up the rotational symmetry in the MFPADs whenever these channels contribute in the same energy region. As for linearly polarized light, the g-u inversion symmetry can also be broken when the $1s\sigma_g$ and $2p\sigma_u$ channels contribute in the same energy region. At photon energies of 20 or 27 eV, there is no breakup of the g-u inversion symmetry since the $2p\sigma_u$ channel does not participate or is barely open and, therefore, has a very small contribution. At 20 eV, the MFPAD does not exhibit rotational symmetry because both $^1\Sigma_u^+$ and $^1\Pi_u$ channels contribute significantly in the whole range of ion kinetic energies. However, at 27 eV, the KE spectrum above 1 eV is entirely dominated by AI from the $^1\Sigma_u^+$ doubly excited states, which preserves the rotational symmetry of the p-like MFPADs along the molecular axis.

At a photon energy of 32.5 eV, the $1s\sigma_g$ and $2p\sigma_u$ ionization channels with both $^1\Sigma_u^+$ and $^1\Pi_u$ symmetries overlap throughout the whole KE spectrum and, consequently, we expect breakups of both g-u inversion and molecular-axis rotational symmetries. As shown in Figs. 2(c) for H_2 and 3(c) for D_2, the comparison between calculated photoionization yields and MFPADs with experiment is good for H_2 and reasonable for D_2. Theoretical MFPADs are averaged over an energy interval of 0.5 eV in order to account for the experimental uncertainty in the fragment energies. It is noticeable from these figures that MFPADs do not in general have inversion

symmetry, except for very low kinetic energies. Additionally, MFPADs in H_2 and D_2 show different shapes, indicating the presence of isotopic effects also in electron angular distributions. Indeed, doubly excited states dissociate more slowly in D_2 than in H_2 and, consequently, the AI process (23) occurs at smaller internuclear distances in D_2 than in H_2. Hence, in D_2, the ionization yield to the $1s\sigma_g$ ($^1\Sigma_u^+$) channel appears at smaller kinetic energies (1–4 eV) than in H_2 [see Fig. 3(c)]. The calculated MFPADs show a rich structure that varies very rapidly with the ion kinetic energy. This variation is more pronounced in D_2. The 0.5 eV average of the calculated MFPADs, performed for a meaningful comparison with the experiment, washes out part of this rapid variation, but significant differences can still be observed when comparing results obtained for different KE values. For H_2, any energy interval chosen to evaluate the average MFPADs leads to a good agreement between theory and experiment. This is also the case for D_2, except around 4.5 eV: any average value calculated by using an energy interval around this value leads to a less satisfactory agreement between theory and experiment than in all previous cases. These noticeable differences in the MFPADs between H_2 and D_2 at the photon energy 32.5 eV indicate differences in the dynamical factors appearing in Eq. (19), i.e., in the magnitudes and phases of the transition amplitudes $C_{\alpha\nu}^{\varepsilon\ell m\mu}$. Consequences in the circular dichroism are yet to be seen in the following.

Figures 4 and 5 show the CDAD [Eq. (3)] for H_2 and D_2, respectively, for the three photon energies considered and for the same selected ion kinetic energies for which MFPADs are displayed in Figs. 2 and 3. As can be seen, the presence of circular dichroism is the normal rule and it can be observed at all polar emission angles θ_e in the YZ plane except for

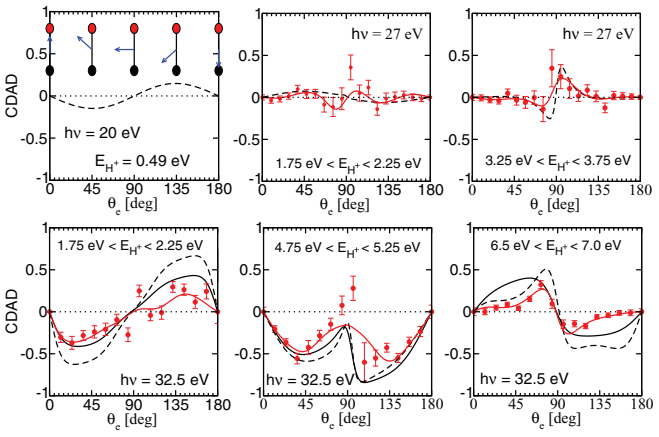

FIG. 4. (Color online) CDAD in H_2 for three photon energies: $\omega = 20$ eV for a fixed proton energy 0.49 eV, $\omega = 27$ eV for proton energies averaged within intervals centered at 2 and 3.5 eV, and $\omega = 32.5$ eV for proton energies averaged within energy intervals centered at 2, 5, and 6.75 eV to account for experimental resolution. Red circles, experimental results; red solid curves, fitting of the experimental results; black solid curves, theoretical results convoluted with the instrumental resolution; black dashed curves, theoretical results. The red balls in the insets denote H^+, and the black ones, H; the blue arrow indicates the electron emission direction with an angle θ_e in the YZ plane.

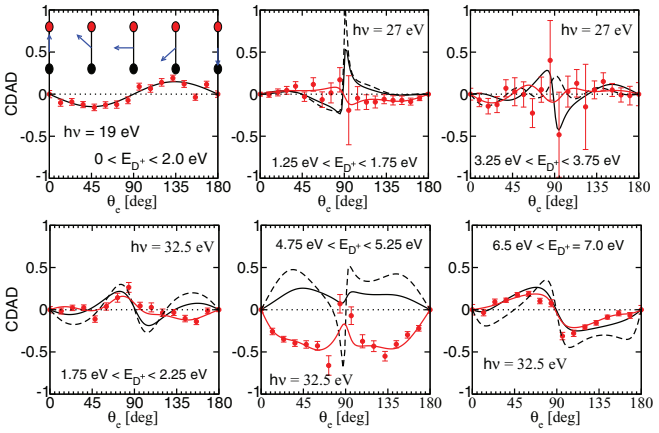

FIG. 5. (Color online) As Fig. 4 but with D_2.

0°, 90°, and 180° for excitation energies of 20 and 27 eV where it vanishes according to the geometry selection rules indicated in the Introduction. Furthermore, CDADs for the photon energy 20 eV are perfectly antisymmetric with respect to 90° at any KE value, a situation which has already been found in other molecules like N_2 [18] and O_2 [22], when only a direct ionization process is involved. At a photon energy of 27 eV, the computed CDADs for H_2 and D_2 are antisymmetric at low ion kinetic energies, but they slightly lose this character at higher kinetic energies. At 27 eV, the CDADs of H_2 and D_2 have opposite phases for ion kinetic energies equal to or above 3 eV (compare the upper right panels in Figs. 4 and 5), which reflects again subtle differences in the imprint of the AI process (23) in the MFPADs of H_2 and D_2. We note that the rapid variation of the CDAD about the 90° polar angle is due to a singularity: indeed in Eq. (3) both the numerator F_{11} and the denominator $2F_{00} + 0.5F_{20} + 3F_{22}$ are about zero at 27 eV, as shown by the MFPADs in Figs. 2(b) and 3(b), so the CDAD at $\theta_e = 90°$ is undefined. Nevertheless, given the size of the experimental error bars at 27 eV and the fact that the CDAD data are close to zero, it is difficult to conclude whether these theoretical predictions are correct.

The most interesting case happens to occur for the photon energy 32.5 eV, where both autoionizing states of the Q_1 and Q_2 series, with dominant contributions of different symmetry, are populated. At low (0–3 eV) and high (6–7 eV) ion kinetic energies, the CDAD plots are nearly antisymmetric with respect to 90° but for intermediate (4–6 eV) KE values the CDAD does not display an antisymmetric character in general. At this photon energy, for kinetic energies between 4 and 6 eV, both DPI and AI processes involving simultaneously the $1s\sigma_g$ and the $2p\sigma_u$ channels leave their signature in the KE spectra and the MFPADs (see the overlapping region in Figs. 2 and 3). In practice, this means that many partial waves contribute to the shape of angular distributions, namely, $1s\sigma_g\sigma_u^{(\ell)}$ with $\ell = 1, 3, 5$, and 7; $2p\sigma_u\sigma_g^{(\ell)}$ with $\ell = 0, 2, 4$, and 6; $1s\sigma_g\pi_u^{(\ell)}$ with $\ell = 1, 3, 5$, and 7; and $2p\sigma_u\pi_g^{(\ell)}$ with $\ell = 2, 4, 6$, and 8. All these angular momenta enter with different amplitudes in Eq. (21) through the coupled angular momentum L_e to build up the coefficients $D_{L_eLN}^{\mu_0}$ in the Legendre expansion for the F_{LN} functions. For instance, the function F_{11}, which is responsible for the CDAD according to Eq. (3), contains the coupling of

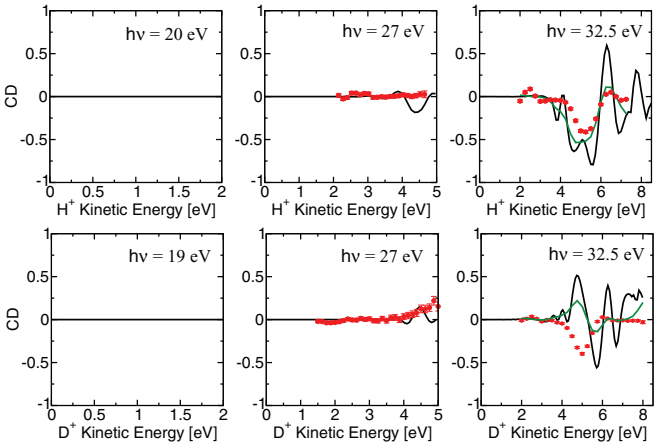

FIG. 6. (Color online) Net circular dichroism according to Eq. (4) associated with MFPADs for H_2 and D_2 against nuclear kinetic energy release, for the three photon energies $\omega = 20$ eV (19 eV for D_2), 27 eV, and 32.5 eV. Red dots, experimental results; black line, theoretical results; green line, theoretical results convoluted with the experimental energy and angular resolution.

16 angular momenta, with L_e running from 0 to 15. An analysis of the individual partial waves contributing in this region does not provide a simple explanation in terms of a few dominant effects. At 32.5 eV, the CDADs of Figs. 4 and 5 simply reflect the complex shapes of the MFPADs shown in Figs. 2 and 3. The most striking case corresponds again to ion kinetic energies around 5 eV, in which a discrepancy between theory and experiment shows up. Experimentally, CDADs for H_2 and D_2 are quite similar and they do not indicate the presence of drastic isotopic effects at this level. In contrast, our theoretical calculations show a change in phase in going from H_2 to D_2 and this effect occurs when the CDAD reaches its larger magnitude. The nice agreement between theory and experiment for H_2 at these intermediate proton kinetic energies makes this question even more puzzling.

Figure 6 shows the net circular dichroism resulting from integration over θ_e of the CDADs as shown in Eq. (4). Due to the prevalent antisymmetry in the CDADs for photon energies 20 and 27 eV, the net computed circular dichroism vanishes except for 27 eV and high ion kinetic energies where small oscillations can be seen in both H_2 and D_2 (note again that the corresponding oscillations are out of phase with respect to each other). In contrast, at 32.5 eV, strong oscillations appear in the CD as a function of the ion kinetic energy. The convoluted theory reproduces very well the oscillations observed in the experimental data for H_2, thus indicating that a net CD exists and it can be measured in homonuclear diatomics [28]. For D_2, the theory and experiment lead to a net CD of opposite sign in the 4–6 eV KE region. The existence of nonzero CD has been identified [28] as the signature of the autoionization of $\mathcal{Q}_1$ and $\mathcal{Q}_2$ doubly excited states into channels of different inversion symmetry (g-u) at different time delays.

A more detailed analysis can be performed at the level of the measured and computed F_{LN} functions that enter in the construction of the MFPADs following Eq. (2). For an overall presentation of the evolution of the F_{LN} functions against the proton KE, and although the content of the information is therefore reduced, we plot in Fig. 7 these F_{LN} functions integrated over the polar angle θ_e as a function of the ion kinetic energy for the photon energy 32.5 eV, for H_2 and D_2. In particular we note that only even terms in the Legendre expansion of the F_{LN} functions according to Eq. (20) take part in the integrals of F_{00}, F_{20}, and F_{22}, whereas only odd terms take part in the integrals of the F_{21} and F_{11} functions. The functions F_{00}, F_{20}, and F_{22} appear in the denominator of the CDAD formula given in Eq. (3); these functions contribute to the total DPI yield in the YZ plane. The function F_{11} appearing in the numerator of Eq. (3) discriminates the angular distributions against the helicity of the incident circularly polarized radiation. The function F_{21} does not enter in the CDAD, but appears when using linearly polarized light in the YZ plane and the polarization vector has a polar angle different from 0° (parallel transitions ${}^1\Sigma_g^+ \rightarrow {}^1\Sigma_u^+$) or 90° (perpendicular transitions ${}^1\Sigma_g^+ \rightarrow {}^1\Pi_u$). F_{21} also mixes contributions from the Σ_u^+ and Π_u components, as F_{11} does. However, it is worth noting that interferences among transition amplitudes build up differently in these two functions due to the phase factor $(-i)^{\delta_{L,1}\delta_{N,1}}$ present in Eq. (21). Theoretical F_{LN} functions for D_2 with N even are in satisfactory agreement with the experimental data and they do not show major differences with those of H_2. In contrast, the comparison between theory and experiment for the F_{11} and F_{21} functions of D_2 is much poorer. For the latter two functions

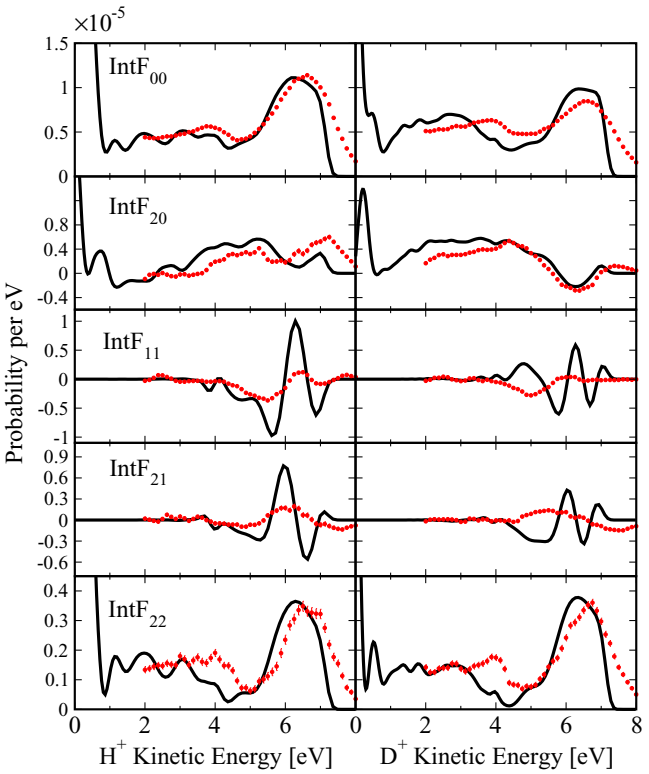

FIG. 7. (Color online) θ_e-integrated F_{LN} functions against the H^+ (D^+) kinetic energy (black curve) for H_2 (left) and D_2 (right) for a photon energy 32.5 eV. Theory, solid lines; experimental results, red dots. These integral functions are obtained with $\mathrm{Int}F_{LN}(E_{\mathrm{H^+(D^+)}}) = \int_0^\pi \sin\theta_e d\theta_e F_{LN}(E_{\mathrm{H^+(D^+)}},\theta_e)$. Experiment and theory are normalized on $\mathrm{Int}F_{00}$ summed in the 2.5–6.5 eV KE range.

of D_2, oscillations in the theoretical and experimental results are in antiphase in the crucial region of ion kinetic energies 4–6 eV. In contrast, theory and experiment are in phase for these same two functions of H_2.

In our theory, the only difference between H_2 and D_2 comes from the solution of the nuclear equation. This is reflected in the integration of electronic dipolar and $\mathcal{Q}H\mathcal{P}$ couplings over the internuclear distance since vibrational wave functions are different for H_2 and D_2. Due to the change of nuclear mass, the number of bound states and the density of vibrational continuum states is larger in D_2 than in H_2. This means in practice that, for the same photon energy, we are not probing the same vibronic states in H_2 and D_2. We discard the role of nonadiabatic couplings on the $\mathcal{Q}_1$ resonances, specifically in the dissociating region after crossing the ionic $1s\sigma_g$ threshold, as being the cause of this discrepancy. Nonadiabatic couplings are not included in our calculations, but nevertheless the comparison between theory and experiment is excellent for H_2. Nonadiabatic couplings are the same for D_2 and for H_2, so there is not a reasonable explanation of why such nonadiabatic effects should play a more important role in D_2. Furthermore, deuterons are slower than protons, so that neglecting nonadiabatic couplings in D_2 should be a better approximation than in H_2. Then we focus on the analysis of the vibrational functions calculated for H_2 and D_2. They are calculated by solving the nuclear equation in a basis set of 240 B splines enclosed within a box of finite size $R_{\max} = 12$ a.u. As the vibrational spacing (density) in D_2 is significantly smaller (larger) than in H_2, we have checked convergence of the D_2 results by enlarging the nuclear box, in steps from $R_{\max} = 9$ to 15 a.u., and also by progressively augmenting the number of B splines. We find out that our calculations are effectively converged with 240 B splines and a box size $R_{\max} = 12$ a.u. Therefore, this cannot be the origin of the discrepancy. Thus the reason for the discrepancy for D_2 at 32.5 eV still remains unknown to us.

VII. CONCLUSIONS

Determination of molecular-frame photoelectron angular distributions of molecules irradiated with polarized light are the subject of current *complete experiments*. In these experiments, measurements probe not only the magnitude of transition matrix elements but also their relative phases. Thus one of the most stringent tests for any theory dealing with the molecular continuum (electronic and nuclear) is to predict electron angular distributions in dissociative photoionization of fixed-in-space molecules in a wide range of energies and molecular orientations. The challenge is more difficult when circularly polarized light is used because the relative phases between molecular states of different symmetries are also probed. In this paper we have faced this challenge and we have systematically investigated, by using the most sophisticated experimental and theoretical tools available to date, molecular-frame photoelectron angular distributions that result from ionization of fixed-in-space H_2 and D_2 molecules with circularly polarized light in a wide range of photon energies. The comparison between theory and experiment has been carried out at the level of ionization yields, MFPADs, and the circular dichroism resulting from the use of different helicities. The comparison has also been performed at the level of the F_{LN} functions entering in the Legendre expansion of the MFPADs, presented here in the form of their integral over the polar angle θ_e. In most cases, theoretical MFPADs, the CD of the angular distributions (CDAD), and net CD are in reasonably good agreement with the experimental results, providing evidence of the crucial role that autoionization and interferences between different ionization channels play in shaping angular distributions. Nevertheless, we have found that isotopic effects (H_2 versus D_2) in MFPADs cannot be fully understood in view of the remaining discrepancies between our theoretical and experimental results at a photon energy of 32.5 eV and ion kinetic energies of about 5 eV, where several photoionization and autoionization channels are open simultaneously. Sources for these discrepancies in D_2 are still unclear to us. We are aware of additional effects that eventually could be relevant in the CD involving homonuclear molecules, such as the role of different symmetries in H_2 and D_2 due to nuclear spin (fermion and boson, respectively) and the related rotational quantum numbers available in both ortho and para species in H_2 and D_2 as well as in the ionic molecular species after photoionization. These statistical effects, which strongly depend on temperature, may bring into the theory additional nuclear phase shifts that, since the molecular dichroism in homonuclear molecules relies on interferences among ionization channels of different inversion symmetry, may play a significant role yet to be explored. Neither temperature nor rotational effects were under such a detailed control in this experiment and then were not included consistently in the theory. More refined experimental measurements and theoretical calculations are thus necessary in order to clarify this puzzling issue.

ACKNOWLEDGMENTS

We are very grateful to L. Nahon and G. Garcia for fruitful cooperation, J. F. Gil for technical support, and the SOLEIL general staff for smoothly operating the facility. We gratefully acknowledge the contribution of S. Lupone and S. Damoy (ISMO). N.S. and D.D. acknowledge the support of the Agence Nationale de la Recherche under ATTOWAVE Contract No. ANR-09-BLAN-0031-01. We also thank Mare Nostrum BSC and CCC-UAM for allocation of computer time. The work was supported by the Spanish Ministerio de Ciencia e Innovación (MICINN) Project No. FIS2010-151127 and ERA-Chemistry Project No. PIM2010EEC-00751, the Spanish Ministerio de Economía y Competitividad (MINECO) Project No. FIS2013-42002-R, the XCHEM Advanced Grant No. GA-290853 of the European Research Council, the European Cooperation in Science and Technology (COST) XLIC Action No. CM1204, and the Vicerrectoría de Investigación at Universidad de Antioquia (CODI Project No. E01538 and Estrategia de Sostenibilidad 2013-2014).

[1] J. C. Tully, R. S. Berry, and B. J. Dalton, Phys. Rev. **176**, 95 (1968).

[2] D. Dill, J. Chem. Phys. **65**, 1130 (1976).

[3] J. Ullrich, R. Moshammer, A. Dorn, R. Dörner, L. P. H. Schmidt, and H. Schmidt-Böcking, Rep. Prog. Phys. **66**, 1463 (2003).

[4] A. Lafosse, M. Lebech, J. C. Brenot, P. M. Guyon, O. Jagutzki, L. Spielberger, M. Vervloet, J. C. Houver, and D. Dowek, Phys. Rev. Lett. **84**, 5987 (2000).

[5] M. Lebech, C. J. Houver, and D. Dowek, Rev. Sci. Instrum. **73**, 1866 (2002).

[6] E. Hecht, *Optics*, 4th ed. (Addison Wesley, Reading, MA, 2002).

[7] G. Garcia, L. Nahon, S. Daly, and I. Powis, Nat. Commun. **4**, 2132 (2013).

[8] M. Pitzer, M. Kunitski, A. S. Johnson, T. Jahnke, H. Sann, F. Sturm, L. P. H. Schmidt, H. Schmidt-Böcking, R. Dörner, J. Stohner *et al.*, Science **341**, 1096 (2013).

[9] G. Schönhense, Phys. Scripta **T31**, 255 (1990).

[10] B. Ritchie, Phys. Rev. A **12**, 567 (1975).

[11] N. A. Cherepkov, Chem. Phys. Lett. **87**, 344 (1982).

[12] R. L. Dubs, S. N. Dixit, and V. McKoy, Phys. Rev. Lett. **54**, 1249 (1985).

[13] N. A. Cherepkov and V. V. Kuznetsov, Z. Phys. D **7**, 271 (1987).

[14] C. Westphal, J. Bansmann, M. Getzlaff, and G. Schönhense, Phys. Rev. Lett. **63**, 151 (1989).

[15] C. Westphal, A. P. Kaduwela, C. S. Fadley, and M. A. VanHove, Phys. Rev. B **50**, 6203 (1994).

[16] K. L. Reid, D. J. Leahy, and R. N. Zare, Phys. Rev. Lett. **68**, 3527 (1992).

[17] S. Motoki, J. Adachi, K. Ito, K. Ishii, K. Soejima, A. Yagishita, S. K. Semenov, and N. A. Cherepkov, J. Phys. B **35**, 3801 (2002).

[18] T. Jahnke, T. Weber, A. L. Landers, A. Knapp, S. Schössler, J. Nickles, S. Kammer, O. Jagutzki, L. Schmidt, A. Czasch *et al.*, Phys. Rev. Lett. **88**, 073002 (2002).

[19] O. Geßner, Y. Hikosaka, B. Zimmermann, A. Hempelmann, R. R. Lucchese, J. H. D. Eland, P.-M. Guyon, and U. Becker, Phys. Rev. Lett. **88**, 193002 (2002).

[20] M. Lebech, J. C. Houver, A. Lafosse, C. Alcaraz, L. Nahon, R. R. Lucchese, and D. Dowek, J. Chem. Phys. **118**, 9653 (2003).

[21] M. Lebech, J. C. Houver, D. Dowek, and R. R. Lucchese, Phys. Rev. Lett. **96**, 073001 (2006).

[22] D. Dowek, M. Lebech, J. Houver, and R. Lucchese, J. Electron Spectrosc. Relat. Phenom. **141**, 211 (2004).

[23] D. Dowek, J. Fernández, M. Lebech, J. C. Houver, and F. Martín, J. Phys.: Conf. Series **88**, 012009 (2007).

[24] D. Dowek, M. Lebech, J. C. Houver, and R. R. Lucchese, Mol. Phys. **105**, 1757 (2007).

[25] W. B. Li, R. Montuoro, J. C. Houver, L. Journel, A. Haouas, M. Simon, R. R. Lucchese, and D. Dowek, Phys. Rev. A **75**, 052718 (2007).

[26] F. Martín, J. Fernández, T. Havermeier, L. Foucar, K. K. Th. Weber, M. Schöffler, L. Schmidt, T. Jahnke, O. Jagutzki, A. Czasch *et al.*, Science **315**, 629 (2007).

[27] J. Fernández and F. Martín, New J. Phys. **11**, 043020 (2009).

[28] D. Dowek, J. F. Pérez-Torres, Y. J. Picard, P. Billaud, C. Elkharrat, J. C. Houver, J. L. Sanz-Vicario, and F. Martín, Phys. Rev. Lett. **104**, 233003 (2010).

[29] J. F. Pérez-Torres, F. Morales, J. L. Sanz-Vicario, and F. Martín, Phys. Rev. A **80**, 011402 (2009).

[30] A. Lafosse, J. C. Brenot, P. M. Guyon, J. C. Houver, A. V. Golovin, M. Lebech, D. Dowek, P. Lin, and R. R. Lucchese, J. Chem. Phys. **117**, 8368 (2002).

[31] R. R. Lucchese, A. Lafosse, J. C. Brenot, P. M. Guyon, J. C. Houver, M. Lebech, G. Raşeev, and D. Dowek, Phys. Rev. A **65**, 020702 (2002).

[32] P. Billaud, M. Géléoc, Y. J. Picard, K. Veyrinas, J. F. Hergott, S. M. Poullain, P. Breger, T. Ruchon, M. Roulliay, F. Delmotte *et al.*, J. Phys. B **45**, 194013 (2012).

[33] R. R. Lucchese, K. Takatsuka, and V. McKoy, Phys. Rep **131**, 147 (1986).

[34] R. E. Stratmann and R. R. Lucchese, J. Chem. Phys **102**, 8493 (1995).

[35] R. E. Stratmann, R. W. Zurales, and R. R. Lucchese, J. Chem. Phys. **104**, 8989 (1996).

[36] M. Yamazaki, J.-I. Adachi, Y. Kimura, M. Stener, P. Decleva, and A. Yagishita, J. Chem. Phys. **133**, 164301 (2010).

[37] C. Bomme, R. Guillemin, T. Marin, L. Journel, T. Marchenko, N. Trcera, R. K. Kushawaha, M. N. Piancastelli, M. Simon, M. Stener *et al.*, J. Phys. B **45**, 194005 (2012).

[38] F. Martín, J. Phys. B **32**, R197 (1999).

[39] J. Fernández, F. L. Yip, T. N. Rescigno, C. W. McCurdy, and F. Martín, Phys. Rev. A **79**, 043409 (2009).

[40] J. L. Sanz-Vicario, H. Bachau, and F. Martín, Phys. Rev. A **73**, 033410 (2006).

[41] R. Zare, J. Chem. Phys. **47**, 204 (1967).

[42] H. Bachau, E. Cormier, P. Decleva, J. E. Hansen, and F. Martín, Rev. Mod. Phys. **64**, 1601 (2001).

[43] I. Sánchez and F. Martín, J. Chem. Phys. **106**, 7720 (1997).

[44] D. Dowek, Y. Picard, P. Billaud, C. Elkharrat, and J. Houver, Chin. J. Chem. Phys. **22**, 178 (2009).

[45] M. Richard-Viard and M. Vervloet, Chem. Phys. **209**, 159 (1996).

[46] A. Lafosse, M. Lebech, J. C. Brenot, P. M. Guyon, L. Spielberger, O. Jagutzki, J. C. Houver, and D. Dowek, J. Phys. B **36**, 4683 (2003).